

Research Article

Cumulative Effect of Pressing and Drying on Stress Generation within a Green Ceramic Compact

E. Vidal-Sallé,¹ D. Falgon,² R. Peczalski,² and J-C. Boyer¹

¹ *Université de Lyon, Institut National des Sciences Appliquées de Lyon, Laboratoire de Mécanique des Contacts et des Structures (LaMCoS), CNRS UMR 5259, Campus de la Doua, bât. Coulomb, 20 Avenue Albert Einstein, 69621 Villeurbanne, France*

² *Université de Lyon, Université Claude Bernard Lyon 1, Laboratoire d'Automatique et de Génie des Procédés (LAGEP), CNRS, UMR 5007, Campus de la Doua, bât. CPE, 3 rue Victor Grignard, 69616 Villeurbanne, France*

Correspondence should be addressed to R. Peczalski; peczalski@lagep.univ-lyon1.fr

Received 14 December 2013; Accepted 29 January 2014; Published 8 April 2014

Academic Editor: Fumio Saito

Copyright © 2014 E. Vidal-Sallé et al. This is an open access article distributed under the Creative Commons Attribution License, which permits unrestricted use, distribution, and reproduction in any medium, provided the original work is properly cited.

The internal stress field induced by uniaxial pressing and subsequent convective drying of a green ceramic powder was simulated by the finite element method. A density dependent elastoplastic constitutive law was used for the mechanical modeling of the compaction. A diffusive water transfer equation and a purely elastic behavior with imposed hydrostrain involving shrinkage were applied for the modeling of the drying process. The key material properties (hydrodiffusivity, hydrocontraction coefficient, Young's modulus, Poisson's ratio, and yield surface parameters) had been experimentally measured and introduced as functions of material density and water content. If residual stresses due to the compaction operation were taken into account, the maximum value of the tensile stress at the top external edge of the wheel and at the beginning of the drying process was two times higher than for a stress free green ceramic compact. Beyond the residual stress onset, the compaction operation induced density heterogeneities which had important consequences on the mechanical behavior of the compact.

1. Introduction

Many factories in the mechanical industry are using grinding wheels for their finishing operations. As these wheels rotate at a high angular velocity, strong centrifugal forces can cause the wheel to break if damaged by initial precrack induced by the elaboration process. For that reason, the grinding wheel manufacturing requires a stringent product quality control.

The grinding wheels dealt with in the present paper are realized with alumina based ceramic. The elaboration is composed of four steps.

- (1) The basic components of the wheel, that is, alumina grains with the primary and secondary binders, are mixed together.
- (2) The wet powder is given a shape using a single action pressing tool. The green ceramic is formed in an annular die and the compression is imposed until reaching the prescribed global density (see Figure 1).

- (3) The wet compact is extracted from the mold and dried with hot air in ventilated chambers at moderate temperature.
- (4) The dry compact is cured (vitrified) in a tunnel oven at a very high temperature; a finishing operation gives the final dimensions of the grinding wheel.

The green ceramic powder is a mix of metal oxide calibrated grains (89% of the total weight) of a mineral compound (10%) which generates glass bonds between grains during curing and of a water based organic compound (1%) which acts as a lubricant during pressing and as a grain primary binder before the curing operation. The small amount of water brought in the product with this binder must be totally eliminated by drying before curing. The drying efficiency has a great influence on the product final quality.

As the manufacturing process induces mechanical strains and stresses within the compact, in some circumstances, dangerous cracks may appear. These cracks appear where the process induced stresses reach the material mechanical

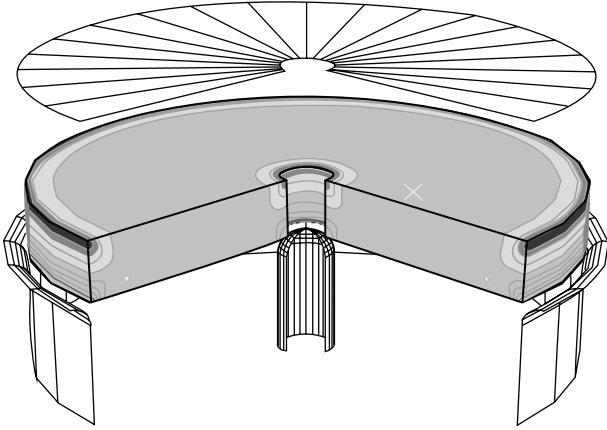


FIGURE 1: Layout of the pressing operation as implemented with Abaqus. The punch (upper plate), the die (cylindrical wall), and the workpiece (annular compact) are drawn. The shades of grey on the compact represent the density levels (the highest density is in black).

strength. They are generally detected at the final quality check of the product but their origin lies in the pre-curing production steps. Several studies concerning similar ceramic materials have pointed out the drying step as the only one responsible for cracking [1–4]. During drying of a wet porous material, volume shrinkage or vapor overpressure may lead to high internal stresses which can induce crack generation. Stresses induced by shrinkage are created at low temperature and low heating rate for materials like clay [1–4] and ceramic powder [5]. Stresses induced by the overpressure, on the contrary, are generated at high temperature and high heating rate for materials like refractory concrete [6, 7]. None of these studies considered the initial mechanical state of a compact generated by a pressing step. It has nevertheless been shown experimentally and numerically [8] that the pressing operation generates a heterogeneous density distribution within an annular compact due to nonuniform friction conditions (see Figure 1). In a subsequent work, it has been shown that the heterogeneous compact exhibited much larger circumferential tensile stress at the top external layer (where the material was denser) than that exhibited by the homogeneous one [9]. The former work has also stipulated that the mechanical behavior of the green ceramic was strongly density dependent. Consequently, density inhomogeneity may induce nonuniform yielding and hardening during the compression which may bring residual stresses on. The heterogeneous and prestressed material may be especially subjected to stress build-up and cracking during drying.

The goal of the present study is to assess how the pressing operation contributes to residual stress generation and failure risk during low temperature convective drying. For this purpose, appropriate compaction and drying models were chosen from the literature and numerically implemented in the finite element solver ABAQUS/Standard. Most of the material properties were determined experimentally. The cracking risk was estimated by comparing the calculated maximal tensile stress and the total equivalent stress to the measured material strength. According to our literature review, such a coupled

analysis of pressing and drying operations applied to a wet cohesive powder was not published yet.

2. Model Development

2.1. Compaction Model. Several constitutive models (stress-strain relations) with different degrees of complexity are available in the literature [8, 10–14] for porous granular materials. In order to choose the appropriate one, it is important to begin by addressing some global issues on the basis of experimental observations. In the case of a green ceramic powder, three major effects have to be considered: elastoplasticity, triaxiality, and strain hardening.

2.1.1. Elastoplastic Behavior. The goal of compaction (pressing) is to increase the bulk density of the product by reducing its volume. The workpiece shape variation implies yielding of the material. But according to direct observation of the industrial pressing process, once the punch was removed (unloading), the compact exhibited a small spring-back. This phenomenon was due to elasticity and the material behavior should thus be considered as elastoplastic. Such assumption implied splitting the total strain rate into an elastic and a plastic component:

$$D_{ij}^t = D_{ij}^e + D_{ij}^p. \quad (1)$$

As the forming process involved large displacements and large strains, the Hencky measure for strains had to be used together with an updated Lagrangian method.

The elastic strain variation $d\epsilon_{ij}^e$ was related to the stress rate according to the generalized Hooke's law:

$$d\epsilon_{ij}^e = -\frac{\nu}{E} d\sigma_{kk} \delta_{ij} + \frac{1+\nu}{E} d\sigma_{ij}, \quad (2)$$

where ν is the *Poisson's* ratio and E is the Young's modulus.

The stress increment objective derivative used here was the classical Jaumann derivative. The determination of the plastic strain variation $d\epsilon_{ij}^p$ was based on the definition of a proper yield surface F and the corresponding yield flow potential G :

$$d\epsilon_{ij}^p = d\lambda \frac{\partial G}{\partial \sigma_{ij}}, \quad (3)$$

where $d\lambda$ was a scalar measuring the amount of plastic flow rate (usually called plastic multiplier). The value of $d\lambda$ was determined by the requirement that plastic deformation proceeds so long as the stress state remains on the yield surface; that is, $F = 0$. The yield function F is defined in Appendix A.

2.1.2. Combined Shear and Triaxial Stress State. The mechanical state of a workpiece during compaction comes from an axial constraint caused by the moving punch, a radial constraint due to the rigid die walls, and a shear load due to friction between the powder and the die walls. This specific loading induces a multiaxial stress state with a deviatoric

(shear) and an isotropic (normal) part that must be considered in the yield and fracture criteria definition.

The compressive plasticity model used here implies a generalized energetic equivalent stress which takes into account the deviatoric part of the stress state (represented by the effective shear stress called also *von Mises* equivalent stress) and also its isotropic part (represented by the mean normal compressive stress p). Such a comprehensive equivalent stress is called below “total equivalent stress”. It is defined in Appendix B and given by

$$\sigma_{\text{eqtot}} = \sqrt{\frac{2(1+\nu)}{3}\sigma_{\text{VM}}^2 + 3(1-2\nu)p^2}, \quad (4)$$

where ν is the Poisson’s ratio, σ_{VM} is the standard *von Mises* equivalent stress, and p is the mean normal compressive stress.

The “total equivalent stress” is a scalar stress value energetically equivalent (strain energy) at a given point to any multidirectional stress state of the material. This “equivalent stress” may be compared to a yield (or ultimate) strength determined by simple uniaxial tensile test in order to determine if plasticity (or fracture) occurs or not. In this study, the “total equivalent stress” was only used as fracture criterion by comparing it to the tensile strength (ultimate strength). The yield criterion was established on the basis of the yield surface F .

2.1.3. Hardening. A multistep compaction test showed the strain hardening induced by the volumetric change (see Figure 2). Consequently, the constitutive behavior must take into account a strain hardening function of the volumetric change. In a pure isotropic (volumetric) regime, the isotropic compression yield stress (p_b) must be a function of ϵ_{kk} , the volumetric strain. The strain hardening due to the deviatoric loads is not easy to quantify so that it is assumed to be negligible.

The Drucker-Prager/Cap model (briefly DP/Cap), which was extensively used for soils [10], can describe such a material behavior [8, 12, 13]. The standard Drucker-Prager yield model is represented in the (p, q) plane by a straight line, where p is the mean normal compressive stress (one third of the first invariant of the stress tensor with a negative sign) and q is the effective shear stress (the square root of the second invariant of the deviatoric stress tensor). The DP/Cap model contains also a “cap” which limits the ability of the material to be compressed (see Figure 3). In other words, the yield surface consists of two main surfaces (see Figure 3): the conical Drucker-Prager “shear failure” surface (F_s) and an elliptical “cap” surface (F_c). The equations of the two surfaces are given in Appendix A. The flow potential G (3) is identical to the yield function F for the “cap” (associated plasticity) but is different from F for the shear failure (nonassociated plasticity) in order to ensure a C^1 continuity when differentiating the flow potential expressions. The expressions of flow potentials G_c and G_s corresponding to the yield surfaces F_c and F_s are given in Appendix A.

When the material yields on the “cap” under compressive stress state, compressive (negative) volumetric plastic strain

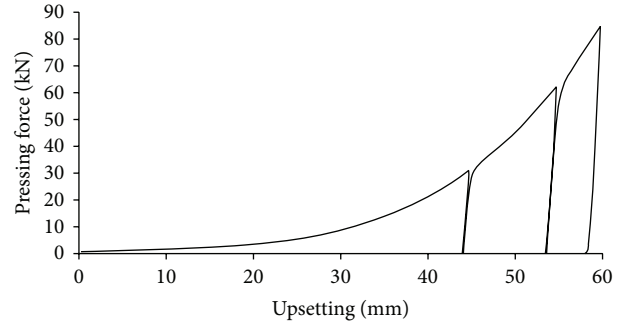


FIGURE 2: Multistep compaction curve for a green ceramic sample at room temperature showing strain hardening.

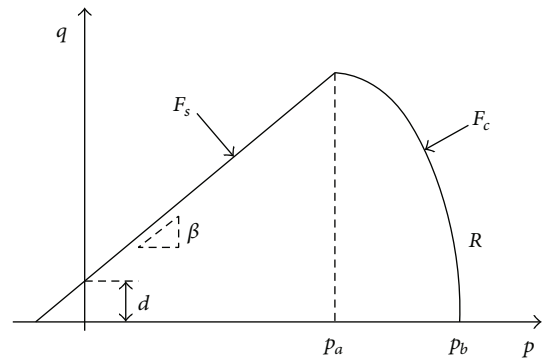


FIGURE 3: Drucker-Prager/Cap yield surface plot: effective shear stress (q) versus mean normal compressive stress (p).

is generated (with density increase), so there is hardening and the “cap” moves right (the isotropic compression yield stress p_b increases). As the cohesion d is a density dependent parameter, its value increases also. When the material yields on the “shear failure” straight line, dilatation (positive) volumetric plastic strain is generated (with density decrease), so there is softening and the “cap” moves left (p_b decreases). Moreover, it was experimentally stated by means of bending tests that cohesion (d) is decreasing with decreasing density. The shear failure surface moves down while the material flows on the “shear failure” line, thus decreasing the shear strength and inducing softening.

2.2. Drying Model. Mechanical tests on dry ceramic powder proved that its behavior was brittle for both compression and bending. So, the material behavior was assumed to be purely elastic with infinitesimal strain during drying. In the general case of porous material thermal dewatering, several physical phenomena can induce specific strain superimposed to the elastic one: thermal dilatation due to temperature rise, hydro contraction due to water loss, and fluid phase overpressure due to water vaporization. In the present case, the thermal and pressure strains were neglected (the temperature rise is moderate and vaporization occurs only at the surface of the compact) and the hydrostrain was related to the linear dry

TABLE 1: Material properties ($[X] = \text{g/kg}$; $[\rho] = \text{kg/m}^3$).

Property	Value or expression
Hydrodiffusivity (D), m^2/s	$(3640 - \rho) * (2.12345e - 4) * \exp(-1.67731e2 * X * 1e - 3)/(3640 * \rho)$
Hydrocontractivity (α), —	0.17
Young's modulus (E), Pa	$21.0877e6 * (\rho * 1e - 3)^{4.66460094} * \exp(-0.1087498 * X)$
Poisson's ratio, —	0.35
Cohesion parameter (d), Pa	$(12100 - 1100 * X) * (\rho * 1e - 3)^{7.9708}$
Isotropic compression yield stress (p_b), Pa [8] (ϵ_{kk}^p —plastic volumetric strain, p_b is basically a function of ρ according to $d\epsilon_{kk}^p = dV/V = d\rho/\rho$)	$A * \exp(B * \epsilon_{kk}^p)$ (1) $0 < \epsilon_{kk}^p < 0.1$, $A = 6639.587243$, $B = 25$ (2) $0.1 < \epsilon_{kk}^p < 0.24$, $A = 8792.066663$, $B = 22$ (3) $0.24 < \epsilon_{kk}^p < 0.95$, $A = 118643.4683$, $B = 11$
Tensile strength (σ_f), Pa	$21375 * (\rho * 1e - 3)^{6.19489} * \exp(-0.2591017 * X)$
Friction angle (β), deg	60
Coulomb's friction coefficient (μ), —	0.25

basis shrinkage coefficient α . The total strain corresponding to a known water content change could be written as

$$d\epsilon_{ij}^t = d\epsilon_{ij}^e + \alpha dX, \quad (5)$$

where X is the material water content (dry basis). As the water content of the ceramic powder was very low, the water was supposed to migrate only by vapor diffusion. The instantaneous water content distribution within the compact was described by Fick's transfer equation:

$$\frac{\partial X}{\partial t} = \vec{\nabla} \cdot (D \vec{\nabla} X), \quad (6)$$

where D was the apparent vapor diffusivity (called hydrodiffusivity in this paper). The surface of the workpiece was supposed in the state of thermodynamic equilibrium with the surrounding air.

2.3. Simulation Conditions

2.3.1. Material Properties. The simulations proposed here were carried out separately for the two operations: compaction and drying. Prior to compaction, the workpiece material was supposed to be isotropic. During the compaction stage, the material was assumed to be elastoplastic following Drucker-Prager/Cap model. Consequently, Young's modulus (E), cohesion parameter (d), isotropic compression yield stress (p_b), and tensile strength (σ_f) were density dependent. For the subsequent drying step, these parameters were also supposed to be water content dependent. During the drying stage, the material mechanical behavior was supposed to be elastic, described by Hooke's model with the (E) and (σ_f) parameters depending on water content and density. In the same manner, the hydrodiffusivity (D) was also water content and density dependent. The other parameters, the hydrocontractivity (α), Poisson's ratio (ν), Coulomb's friction coefficient (μ), and the friction angle (β) (the slope of the straight line of the Drucker-Prager law), were supposed to be constant. All the material properties parametric laws used for simulations are summarized in Table 1.

Young's modulus (E) was determined from the slope of the stress versus strain curve recorded during free compression of cylindrical samples (prepared at different densities and water contents) on a mechanical testing machine (see Figure 4). Tensile strength (σ_f) was directly measured on the same machine by four points bending of parallelepipedic samples prepared at different densities and water contents (see Figure 4). Poisson's ratio was determined by measuring the radial and axial deformation by means of strain gauges attached to a cylindrical sample submitted to free compression (see above). The cohesion parameter (d), the isotropic compression yield stress (p_b), the friction coefficient (μ), and the friction angle (β) were identified by the best fit between the experimental and simulated force versus punch displacement curves during confined axial compaction in a cylindrical die [8].

The hydrodiffusivity (D) was identified by fitting measured water loss curves for a cylindrical sample dried in a climatic oven by a simplified solution of a diffusive internal water transfer model. The hydrocontractivity (α) was determined by measuring with optical sensors the radius and height variations of a cylindrical sample during drying in an oven.

The overall accuracy of the measurements was close to 15%. The values given in Table 1 were obtained for material water content (X) ranging from 3 g/kg to 10 g/kg and for material density (ρ) ranging from 1900 kg/m³ to 2500 kg/m³. These ranges corresponded to the real values involved in industrial product processing.

2.3.2. Boundary and Initial Conditions for Compaction. The die and the punch corresponded to axisymmetric rigid walls with a Coulomb friction applied at the interface with the annular workpiece (see Figure 1). Even if there was no water content and no temperature changes during the compression, thermomechanical 4 node axisymmetric elements (CAX4T) were used in Abaqus implementation in order to realize the drying simulation after the compaction and ejection of the workpiece using the same geometrical model. The material

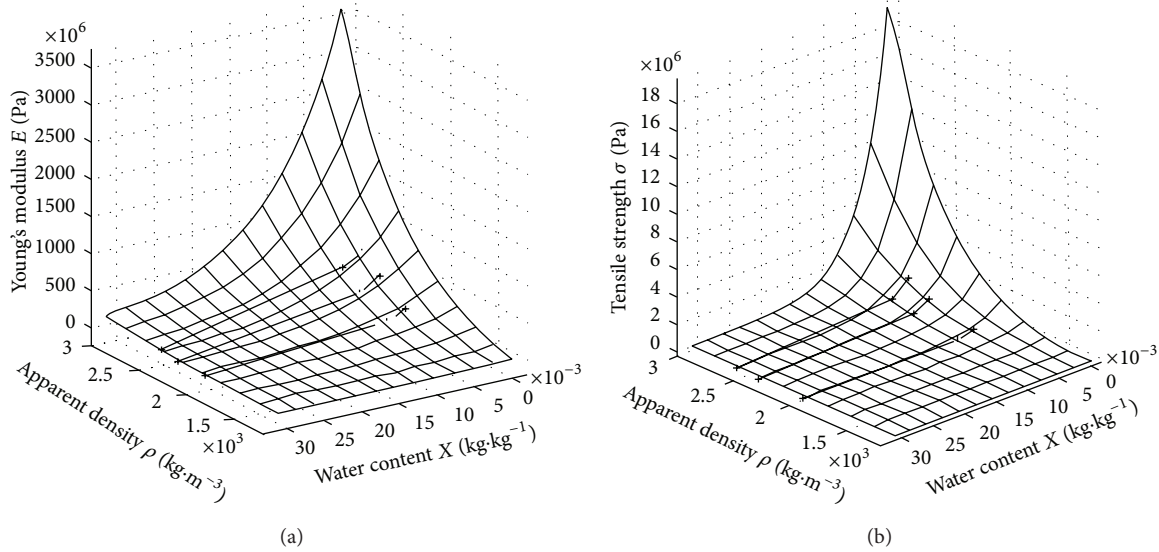


FIGURE 4: Young's modulus (a) and tensile strength (b) versus density and water content (the black crosses are experimental points; the grey curves represent the fitted surface).

was not strain rate dependent, so the punch velocity was not relevant information. The initial density was about 1250 kg/m^3 and the final one was 2200 kg/m^3 in the core of the product. After the compression, the unloading and ejection of the compacted workpiece were simulated and led to the initial state before drying.

2.3.3. *Boundary and Initial Conditions for Drying.* As the compact lied on a flat plate, its bottom face was considered impermeable (no water flux in axial direction). The mechanical boundary conditions were more questionable but, in the present work, it was assumed that the lower face of the compact did not leave its support (no vertical displacement). The initial water content was supposed to be uniform within the compact at a value of 10 g/kg . The surface equilibrium water content was set equal to 10 g/kg in the ambient air and to 3 g/kg inside the oven. Two transition periods between room and oven climatic conditions were considered: 10 seconds or 5 minutes. The surface equilibrium water content was assumed to vary linearly from 10 to 3 g/kg over the transition period.

3. Simulations Results and Discussion

3.1. *Mechanical State of the Compact after Pressing.* The simulated density distributions and stress fields within a compacted ring after the pressing process (after unloading and pulling the ring out of the die) are presented in Figures 5 to 7. The compacts were obtained by axial single action pressing with a ratio of the final to the initial height of 50%. The finite element predictions of the fields are plotted as isovalue lines, with the minimum and the maximum values indicated, respectively, by a dot and an asterisk.

According to Figure 5, the material density is quite uniform in the core of the compact, whereas noticeable density gradients take place at the four edges of the axial

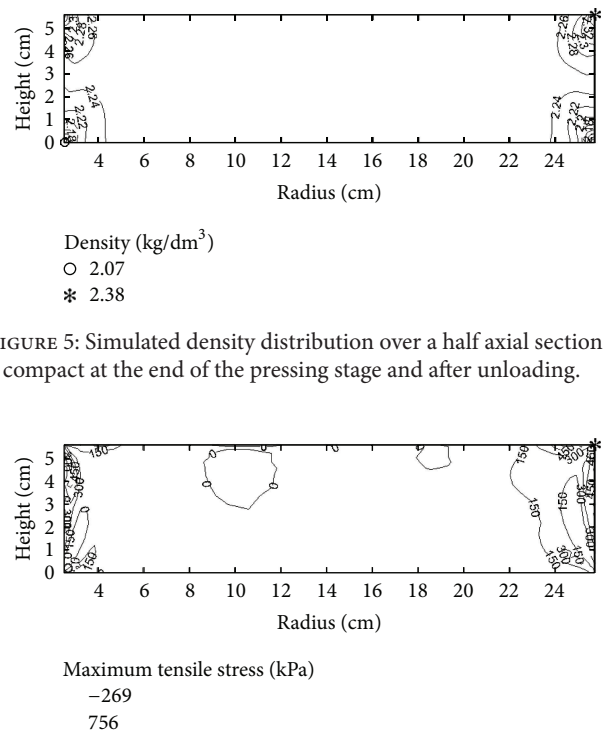


FIGURE 5: Simulated density distribution over a half axial section of a compact at the end of the pressing stage and after unloading.

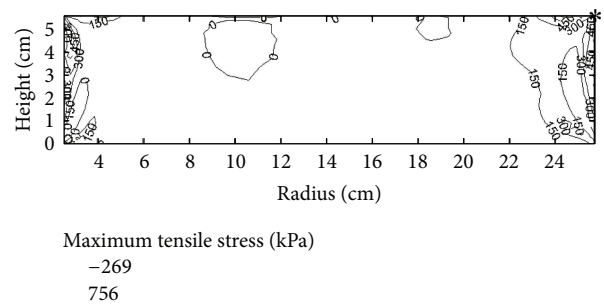


FIGURE 6: Simulated maximum tensile stress distribution over a half axial section of a compact at the end of the pressing stage and after unloading.

section. The lowest density value, roughly 90% of the mean core value, is found at the bottom external edge, while the highest one, roughly 110% of the mean core value, stands at the top external edge. These simulation results were validated experimentally [8] using the colored layers technique. Similar density distributions within cylindrical compacts of ceramic

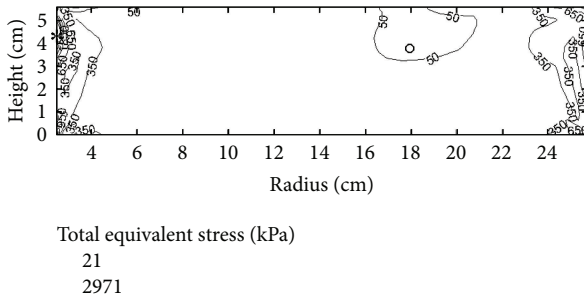


FIGURE 7: Simulated total equivalent stress distribution over a half axial section of a compact at the end of the pressing stage and after unloading.

or pharmaceutical powders are reported in the literature [15, 16]. The heterogeneity of the powder comes from the friction that slows down the movement of the particles at the lower corners of the ring and packs the particles of the upper corners more than the particles which are far away from the die vertical surface.

Maximum tensile stress was evaluated as it is a common strength criterion for brittle materials. According to Figure 6, the distribution of the first eigenvalue of the Cauchy stress tensor, that is, the maximum tensile stress, exhibits qualitatively a similar pattern to the density field's one. Such result was expected as the main load corresponds to a volumetric change (i.e., a density change). Strong gradients are located near the internal and external lateral borders of the compact, with the maximum value located at the external top edge. During the pressing process, friction between the vertical surface of the die and the ceramic particles induces different volumetric plastic strain in the vicinity of the vertical external surfaces of the ring. These plastic strain gradients are the outset of the internal stresses.

As written in the preceding section, the great compressive plasticity which occurs during the compaction can lead to using the total equivalent stress to estimate the intensity of the residual loading. The total equivalent stress field after unloading is shown in Figure 7. Minima and maxima of residual stresses are also found on the internal and external faces of the ring with similar values in both faces. The minimum stress found in the upper face is not very significant and can be explained by the differences between friction stresses along the surface.

The high value of this equivalent stress on the internal radius of the ring is related to a high compressive mean stress in this area. The analysis of the failure risk must consider the sign of the mean normal stress: a positive one corresponds to a dangerous isotropic tension while a negative one to a conservative isotropic pressure.

3.2. Mechanical State of the Compact during Drying. The results of the following simulation cases are presented.

Case 1. Drying of a homogeneous (uniform density) and residual stress free compact.

Case 2. Drying of a heterogeneous stress free compact, the density field applied is the one predicted by simulation at the end of the pressing step (and after demolding).

Case 3. Drying of a heterogeneous compact with the density and residual stress distributions predicted at the end of the pressing step as initial conditions (after demolding).

The total equivalent stress, the maximum tensile stress, and the material tensile strength at the external radius top edge of the compact are plotted as a function of the drying time on Figures 8 to 10 (Figure 8 corresponds to Case 1, Figure 9 to Case 2, and Figure 10 to Case 3). The considered location corresponds to the most loaded zone of the compact. The stresses and material strength are given for 2 integration points, A and B, in the same finite element located at the right top corner of the compact axial section. Point A is situated at 0.8 mm from the top surface and at 1.4 mm from the lateral one; point B is situated at 0.2 mm from the top surface and at 0.4 mm from the lateral one.

The material tensile strength rises with increasing density and with decreasing water content (see Table 1). The strength is increasing with time because water content is decreasing as drying proceeds. The material strength at the right upper corner of the ring for the homogeneous sample (Case 1), where the local density is equal to the mean value in the ring, is lower than for the heterogeneous sample (Cases 2 and 3) where, due to pressing effects, much higher values are induced for Cases 2 and 3. The material strength at point B is always greater than that at point A because in this part of the compact the density increases toward the surface.

Nevertheless, for the considered conditions and for Case 1 (see Figure 8), the stress state reached at the end of drying is always smaller than the material strength. Consequently, the drying operation seems to be correctly designed. The same conclusions can be drawn observing Case 2 where only the density heterogeneity is taken into account. Case 3 is less simple to analyze. At point B, the stresses for Case 3 are nearly 1.3 times higher than for Case 2 and nearly 2.5 times higher than for Case 1. It shows the influence of both density gradients and residual stresses on the final state of stress. Nevertheless, considering point A, conclusions are not so easy. At point A, the stresses for Case 2 are higher than for Case 1, but the stresses for Case 3 are almost the same than for Case 1. These apparently diverging results may be explained by the very huge density, water content, and consequently stress gradients near the surface of the workpiece and especially in the external top corner where the points A and B are located.

The general trends brought to light by these simulations results study may be easily interpreted considering that the key material hydromechanical properties depend strongly on density and water content. The hydrodiffusivity, which governs water transfer rate and thus hydrostrain gradient magnitude, increases with decreasing density and with decreasing water content (see Table 1). Young's modulus, which governs stress generation for a given hydrostrain gradient, increases with increasing density and with decreasing water content (see Table 1).

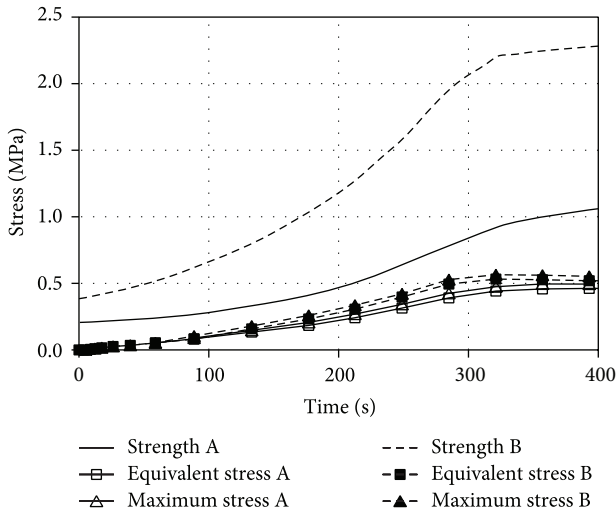


FIGURE 8: Case 1: Total equivalent stress and tensile strength during drying of a homogeneous (uniform density) and residual stress free compact.

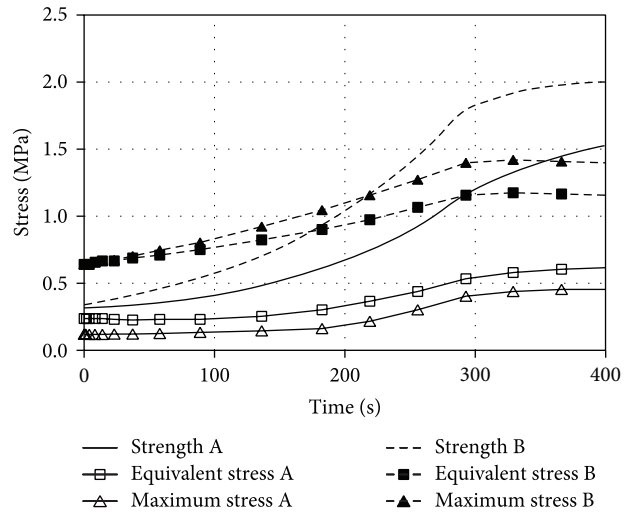


FIGURE 10: Case 3: Total equivalent stress and tensile strength during drying of a real compact (the simulated pressing induced density and residual stress distributions were used as initial conditions).

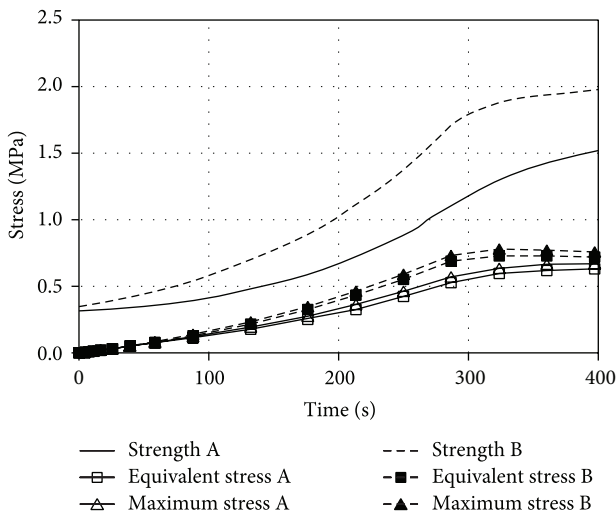


FIGURE 9: Case 2: Total equivalent stress and tensile strength during drying of a heterogeneous (the simulated pressing induced density distribution was used as initial condition) and residual stress free compact.

Case 2 (see Figure 9) reflects the influence of compaction induced density gradients. The density peaks are located at the external radius top edge of the compact where, consequently, the vapor diffusivity is decreased and Young's modulus is increased. The low diffusivity level enhances water content gradients and therefore enhances hydrostrain gradients. High Young's modulus level enhances stress generated by hydrostrain gradients. At the compact densest locations, both the vapor diffusivity and Young's modulus dependence on the density are amplifying stress. This effect is weakened by vapor diffusivity increase with decreasing water content. At the compact external locations, the vapor diffusivity and consequently the water content gradients are decreasing as drying proceeds.

Case 3 (see Figure 10) reflects the influence of both density peaks and residual stress induced by compaction. The maximal tensile stress at the external radius top edge is roughly the sum of the stress calculated for Case 2 and that calculated at the end of pressing. For Cases 1 and 2, the stress remains fairly below the strength, but for Case 3 the stresses reach the material strength at the very beginning of the drying process.

The total equivalent stress is very close to the maximal tensile stress for Cases 1 and 2. For Case 3, a difference exists and is increasing with time. Consequently, the duration of strength overcoming is 180 seconds for the equivalent stress and 220 seconds for the maximal stress. The main difference between Cases 1 and 2 on one hand and Case 3 on the other hand stands in the presence of compaction residual stresses. These stresses are basically volumetric ones. Only the total equivalent stress is able to take into account such a quantity. It is not thus surprising that, for the only simulation which takes into account volumetric changes, a difference exists between the maximum tensile stress and the total equivalent stress. This difference shows the influence of volumetric changes on the stress state of the compact. Neglecting volumetric changes might lead to the underestimation of the load.

Besides the stress and density distribution generated by pressing, the rate of climatic conditions variation during the starting-up period of the drying oven was expected to impact the stress level in superficial layers of the compact. This influence was analyzed by simulating the drying step for different climatic transition periods. The climatic transition period is the time needed for reaching constant hydrothermal conditions at the compact surface. That corresponds in industrial practice to different oven loading and oven start-up times. In an early paper [17], a strong impact of climatic transition duration was shown, but without considering the variation of hydrodiffusivity and Young's modulus with water content. In the present work, all key properties are both

density and water content dependent and the influence of the climatic transition appeared practically negligible (results are not shown). The shorter is the climatic transition, the stronger are the superficial water content gradient and initial drying rate, but as the water content decreases very quickly, the hydrodiffusivity increases greatly and this results finally in water content gradient flattening and hydrostrain decreasing.

4. Conclusions

According to this study, the manufacture of a piece of green ceramic powder by unidirectional pressing in a rigid annular die generated density gradients, plastic strains, and residual stresses within the compacted sample. For the particular conditions considered here, the density gradients were most pronounced at the top external radius edge where the density rose up to 110% of the mean core value. At the same location, the stress level was the highest and the maximum tensile stress rose up to 500% of the mean core value.

During the drying process of ceramic compacts (usually by hot air stowing), tensile stress arises in the external layers of the product. In the case studied, the residual stresses induced by prior pressing were added to the drying induced ones. For this reason, at the early beginning of the drying process, the cumulated maximum tensile stress was twice higher at the top external edge for a real compact affected by prior pressing than for a fictive homogeneous compact without pressing impact. The material strength was reached in the former case, but only in a very thin superficial layer. The pressing process of agglomerate compacts may thus be responsible for skin cracks during the drying process because of the cumulative effect of the two processes on the internal stress build-up. On ceramics production lines, it is a matter of fact that most of the cracks appear at the top external radius edge of the annular compacts. Not all the superficial cracks will damage the compact. When the critical zone is very thin, the cracks in a noncohesive material do not propagate and may be eliminated during the finishing.

Once validated, the computer model developed in this study can be used for the search of optimal manufacturing conditions which guarantee a crack free product with maximal throughput ratio and/or minimal energy consumption. This work concerned directly vitrified ceramics, but it has a larger application since drying induced cracking affects many products like concrete, clay, wood, and pharmaceuticals.

Appendices

A. Yield Surface and Flow Potential

The equations for the yield surface and yield flow potential corresponding to the Drucker-Prager/Cap model are given below with the definitions of the different parameters:

p —mean normal compressive stress, $p = -(1/3) \text{tr}(\underline{\underline{\sigma}})$ where $\underline{\underline{\sigma}}$ is the Cauchy stress tensor;

q —effective shear stress (square root of the second invariant of the deviatoric stress), $q^2 = (3/2)s_{ij}s_{ij}$ where s_{ij} are the components of the deviatoric stress tensor;

F_s —“shear failure” surface, $F_s = q - p \tan \beta - d = 0$, β and d are defined in Figure 3;

F_c —“cap” surface, $F_c = \sqrt{(p - p_a)^2 + [Rq/(1 + \alpha - (\alpha/\cos \beta))]^2} - R(d + p_a \tan \beta) = 0$, p_a is defined in Figure 3. R corresponds to the radius of the cap and α is a parameter which ensures a C^1 continuity of the model;

F_t —“transition” surface, $F_t = \sqrt{(p - p_a)^2 + [q - (1 - (\alpha/\cos \beta))(d + p_a \tan \beta)]^2} - \alpha(d + p_a \tan \beta) = 0$;

Flow potentials: $G_s = \sqrt{[(p - p_a) \tan \beta]^2 + [q/(1 + \alpha - (\alpha/\cos \beta))]^2}$ and $G_c = \sqrt{(p - p_a)^2 + [Rq/(1 + \alpha - (\alpha/\cos \beta))]^2}$.

B. Total Equivalent Stress

The development of the expression for the total equivalent stress is given in this section.

The specific strain energy for infinitesimal transformation is equal to

$$\frac{\sigma_{ij}\varepsilon_{ij}}{\rho} \quad (\text{B.1})$$

For a known density, this strain energy can be split in a deviatoric part and a purely volumetric one:

$$\sigma_{ij}\varepsilon_{ij} = s_{ij}e_{ij} + \frac{\sigma_{kk}\varepsilon_{kk}}{3}, \quad (\text{B.2})$$

where s_{ij} and e_{ij} are, respectively, the stress and strain deviatoric tensors.

Introducing the generalized Hooke's law, the elastic strain energy can be expressed as a function of s_{ij} and p (the mean normal stress pressure):

$$s_{ij}e_{ij} = \frac{1 + \nu}{E} s_{ij}s_{ij}, \quad (\text{B.3})$$

$$\frac{\sigma_{kk}\varepsilon_{kk}}{3} = \frac{3(1 - 2\nu)}{E} p^2.$$

Let us now write the same quantities for a unidirectional tensile test:

$$s_{ij}e_{ij} = \frac{1 + \nu}{E} \frac{2}{3} \sigma_T^2, \quad (\text{B.4})$$

$$\frac{\sigma_{kk}\varepsilon_{kk}}{3} = \frac{1 - 2\nu}{3E} \sigma_T^2.$$

So, $((1 + \nu)/E)s_{ij}s_{ij} + (3(1 - 2\nu)/E)p^2$ the total strain energy of any stress state can be compared to the strain energy of the tensile stress state: $((1 + \nu)/E)(2/3)\sigma_T^2 + ((1 - 2\nu)/3E)\sigma_T^2$.

Consequently, the “total equivalent stress” can be defined as

$$\sigma_{\text{eqtot}} = \sqrt{\frac{2(1 + \nu)}{3} \sigma_{\text{VM}}^2 + 3(1 - 2\nu) p^2}. \quad (\text{B.5})$$

Conflict of Interests

The authors declare that there is no conflict of interests regarding the publication of this paper.

Acknowledgments

This work was financially supported by two French governmental agencies: "Agence pour le Développement et la Maîtrise de l'Énergie" (ADEME) and "Agence Nationale de la Recherche Technique" (ANRT).

References

- [1] G. Musielak, "Internal stresses caused by outflow of moisture and phase change inside dried material," *Drying Technology*, vol. 14, no. 2, pp. 289–306, 1996.
- [2] S. J. Kowalski, G. Musielak, and A. Rybicki, "The response of dried materials to drying conditions," *International Journal of Heat and Mass Transfer*, vol. 40, no. 5, pp. 1217–1226, 1997.
- [3] J. Banaszak and S. J. Kowalski, "Theoretical and experimental analysis of stresses and fractures in clay like materials during drying," *Chemical Engineering and Processing: Process Intensification*, vol. 44, no. 4, pp. 497–503, 2005.
- [4] Y. Itaya, S. Mabuchi, and M. Hasatani, "Deformation behavior of ceramic slabs by nonuniform drying," *Drying Technology*, vol. 13, no. 3, pp. 801–819, 1995.
- [5] R. Peczalski, P. Laurent, J. Andrieu, J. C. Boyer, and M. Boivin, "Drying-induced cracking of abrasive rings: risk prediction and process optimisation by numerical simulation," *Drying Technology*, vol. 14, no. 2, pp. 333–348, 1996.
- [6] Z.-X. Gong and A. S. Mujumdar, "Development of drying schedules for one-side-heating drying of refractory concrete slabs based on a finite element model," *Journal of the American Ceramic Society*, vol. 79, no. 6, pp. 1649–1658, 1996.
- [7] Z.-X. Gong and A. S. Mujumdar, "A two-dimensional finite element model for kiln-drying of refractory concrete," *Drying Technology*, vol. 13, no. 3, pp. 585–605, 1995.
- [8] D. Falgon, E. Vidal-Sallé, J.-C. Boyer, R. Peczalski, and J. Andrieu, "Identification procedure of a hardening law for powder compaction," *Powder Technology*, vol. 157, no. 1–3, pp. 183–190, 2005.
- [9] R. Peczalski, D. Falgon, J. Andrieu, J.-C. Boyer, and E. Vidal-Sallé, "Impact of density gradients on the stress level within a green ceramic compact during drying," *Drying Technology*, vol. 23, no. 1–2, pp. 71–82, 2005.
- [10] M. L. Baron, I. Nelson, and I. Sandler, "Influence of constitutive models on ground motion predictions," *Journal of the Engineering Mechanics Division*, vol. 99, no. 6, pp. 1181–1200, 1973.
- [11] D. Bortzmeyer, "Modelling ceramic powder compaction," *Powder Technology*, vol. 70, no. 2, pp. 131–139, 1992.
- [12] I. Aydin, B. J. Briscoe, and N. Ozkan, "Modeling of powder compaction: a review," *Materials Research Society Bulletin*, vol. 22, no. 12, pp. 45–51, 1997.
- [13] I. Aydin, B. J. Briscoe, and K. Y. Sanliturk, "Dimensional variation of die-pressed ceramic green compacts: comparison of a finite element modelling with experiment," *Journal of the European Ceramic Society*, vol. 17, no. 10, pp. 1201–1212, 1997.
- [14] H. Zipse, "Finite-element simulation of the die pressing and sintering of a ceramic component," *Journal of the European Ceramic Society*, vol. 17, no. 14, pp. 1707–1713, 1997.
- [15] N. Özkan and B. J. Briscoe, "Characterization of die-pressed green compacts," *Journal of the European Ceramic Society*, vol. 17, no. 5, pp. 697–711, 1997.
- [16] K. T. Kim, S. W. Choi, and H. Park, "Densification behavior of ceramic powder under cold compaction," *Journal of Engineering Materials and Technology*, vol. 122, no. 2, pp. 238–244, 2000.
- [17] F. L. di Maggio and I. S. Sandler, "Material model for granular soils," *Journal of the Engineering Mechanics Division*, vol. 97, no. 3, pp. 935–950, 1971.



Hindawi

Submit your manuscripts at
<http://www.hindawi.com>

